

Search for magnetic monopoles produced via the Schwinger mechanism

<https://doi.org/10.1038/s41586-021-04298-1>

Received: 18 June 2021

Accepted: 1 December 2021

Published online: 2 February 2022

 Check for updates

B. Acharya¹, J. Alexandre¹, P. Benes², B. Bergmann², S. Bertolucci³, A. Bevan⁴, H. Branzas⁵, P. Burian², M. Campbell⁶, Y. M. Cho⁷, M. de Montigny⁸, A. De Roeck⁶, J. R. Ellis^{1,9}, M. El Sawy⁶, M. Fairbairn¹, D. Felea⁵, M. Frank¹⁰, O. Gould^{11,12}, J. Hays⁴, A. M. Hirt¹³, D. L.-J. Ho¹⁴, P. Q. Hung¹⁵, J. Janecek², M. Kalliokoski¹², A. Korzenev¹⁶, D. H. Lacarrère⁶, C. Leroy¹⁷, G. Levi^{3,18}, A. Lioni¹⁶, A. Maulik^{3,8}, A. Margiotta¹⁸, N. Mauri³, N. E. Mavromatos¹, P. Mermod^{16,25}, L. Millward⁴, V. A. Mitsou¹⁹, I. Ostrovskiy²⁰, P.-P. Ouimet⁸, J. Papavassiliou¹⁹, B. Parker²¹, L. Patrizii³, G. E. Pávālaš⁵, J. L. Pinfold⁸, L. A. Popa⁵, V. Popa⁵, M. Pozzato³, S. Pospisil², A. Rajantie¹⁴, R. Ruiz de Austri¹⁹, Z. Sahnoun³, M. Sakellariadou¹, A. Santra¹⁹, S. Sarkar¹, G. Semenoff²², A. Shaa⁸, G. Sirri³, K. Sliwa²³, R. Soluk⁸, M. Spurio¹⁸, M. Staelens⁸, M. Suk², M. Tenti²⁴, V. Togo³, J. A. Tuszynski⁸, A. Upreti²⁰, V. Vento¹⁹ & O. Vives¹⁹

Electrically charged particles can be created by the decay of strong enough electric fields, a phenomenon known as the Schwinger mechanism¹. By electromagnetic duality, a sufficiently strong magnetic field would similarly produce magnetic monopoles, if they exist². Magnetic monopoles are hypothetical fundamental particles that are predicted by several theories beyond the standard model^{3–7} but have never been experimentally detected. Searching for the existence of magnetic monopoles via the Schwinger mechanism has not yet been attempted, but it is advantageous, owing to the possibility of calculating its rate through semi-classical techniques without perturbation theory, as well as that the production of the magnetic monopoles should be enhanced by their finite size^{8,9} and strong coupling to photons^{2,10}. Here we present a search for magnetic monopole production by the Schwinger mechanism in Pb–Pb heavy ion collisions at the Large Hadron Collider, producing the strongest known magnetic fields in the current Universe¹¹. It was conducted by the MoEDAL experiment, whose trapping detectors were exposed to 0.235 per nanobarn, or approximately 1.8×10^9 , of Pb–Pb collisions with 5.02-teraelectronvolt center-of-mass energy per collision in November 2018. A superconducting quantum interference device (SQUID) magnetometer scanned the trapping detectors of MoEDAL for the presence of magnetic charge, which would induce a persistent current in the SQUID. Magnetic monopoles with integer Dirac charges of 1, 2 and 3 and masses up to 75 gigaelectronvolts per speed of light squared were excluded by the analysis at the 95% confidence level. This provides a lower mass limit for finite-size magnetic monopoles from a collider search and greatly extends previous mass bounds.

Magnetic monopoles (MMs) are hypothetical fundamental particles that carry isolated magnetic charge—that is, a single north or south pole. Their existence would symmetrize the Maxwell equations of electrodynamics via a duality transformation. Dirac formulated the first field theory of a point-like magnetic charge interacting with quantum charged matter and showed³ that the existence of an MM would necessitate the quantization of electric charge. This important result, known as the Dirac quantization condition (DQC), is given by

$$\frac{eg}{2\pi} = n\hbar \rightarrow g = ng_D = n \frac{2\pi\hbar}{e}, \quad (1)$$

where g_D is the unit Dirac charge, e is the electric charge, g is the magnetic charge, \hbar is the reduced Planck's constant and n is an integer. Dirac's theory describes the MM as an elementary particle with its mass as a free parameter, to be constrained by experiments¹². MMs also appear as solutions of grand unified theories (GUTs)^{4,5}. In contrast to the Dirac monopole, GUT MMs are composites of the fundamental non-Abelian gauge and Higgs fields that characterize the theory. Their expected masses are close to the GUT scale (10^{16} GeV/ c^2 ; c , speed of light in a vacuum) and thus cannot be produced in a realistic collider experiment. Moreover, GUT MMs are expected to have been diluted by cosmic inflation, and hence it is unlikely that they will be observed

even in cosmic ray searches. In fact, the theory of GUT MMs motivated the idea of an inflationary Universe¹³. String theories also predict MMs⁶, which may have masses much lower than the GUT scale, depending on the string scale. The composite MMs, as opposed to the point-like Dirac ones, would have an internal structure. These models arise from spontaneously broken gauge theories, and in recent years composite finite-energy MM solutions were also discovered in various field theories beyond the Standard Model, possibly with masses as low as a few TeV⁷. This raises the prospects for collider production of such objects, thus reviving interest in experimental searches for MMs.

All searches for the direct production of MMs at particle accelerators so far have focused on collisions of elementary particles such as electrons—or quarks in the case of hadron collisions—assuming production via fermion–antifermion annihilation (the Drell–Yan mechanism) or photon–photon collisions. However, the strong coupling of the MM, arising from equation (1)³, makes it difficult to calculate the production cross-section. Indeed, it has been argued that the production of composite MMs from elementary particle collisions is exponentially suppressed by $e^{-4/\alpha}$, where α is the electromagnetic fine structure constant^{14,15}. This exponential suppression can be interpreted as a consequence of the large physical size of the monopole relative to its Compton wavelength, and hence the small overlap of initial and final states. Alternatively, it can be seen as due to the low relative entropy of the specific coherent state of a composite monopole, in comparison to other configurations comprising the same large number of particles. However, it is not known what a purely nonperturbative treatment, which is still lacking, would imply. Collider experiments have nevertheless focused on interpreting searches in the context of point-like MMs¹⁶, whereas most MMs predicted by models considered in the literature are composite objects, including the light MMs potentially accessible at the Large Hadron Collider (LHC)^{17–23}.

A way to avoid these shortcomings is provided by searching for MM pair production via the Schwinger mechanism. In 1951, building upon earlier work by Sauter, Euler and Heisenberg^{24,25}, Schwinger¹ showed that electrically charged particles could be produced by the decay of a strong electric field. If MMs exist, electromagnetic duality, supported by explicit calculations^{2,9}, implies that they would also be produced by the same mechanism in a sufficiently strong magnetic field. Unprecedented magnetic fields are present, fleetingly, in ultraperipheral heavy-ion collisions¹¹. In this case, the MM production cross-section can be computed without relying on perturbation theory (that is, non-perturbatively) using semiclassical techniques, including the effects of strong MM–photon coupling. Owing to the coherence of the magnetic field over length scales comparable to the monopole size, the overlap of initial and final states is not suppressed exponentially by $e^{-4/\alpha}$, as in the collision of point-like particles. The magnetic field also overcomes the entropic argument for this suppression, because it makes MM production preferential over the production of an arbitrary state with the same number of particles. Indeed, in this approach, the finite size^{8,9} and strong coupling of MMs^{2,10} enhance their production by decreasing the semiclassical barrier. For example, in constant fields, these effects can increase the MM mass reach by an order of magnitude.

Although Schwinger production of MMs in a constant, or slowly varying, magnetic field is well understood theoretically, and the production probability has been calculated accurately from first principles^{2,9}, the strong space and time dependence of the electromagnetic fields of LHC heavy-ion collisions present additional theoretical challenges. Progress on this front is made possible owing to the large charges of heavy ions, as a consequence of which the resulting electromagnetic field can be approximated as a coherent classical field sourced by the charge distribution of the ions. The strongest fields are generated in ultraperipheral collisions, for which the impact parameter is approximately twice the nuclear radius. In the 2018 heavy-ion run at the LHC, the peak magnetic field strength was $B \approx 10^{16}$ T (ref. 11), with an inverse decay time $\omega \approx 10^{26}$ s⁻¹. This field strength is about seven orders of magnitude

greater than the critical field strength of quantum electrodynamics, and more than four orders of magnitude greater than the strongest known astrophysical magnetic fields, which are present on the surfaces of magnetars²⁶. The probability of MM pair production by the Schwinger mechanism depends strongly on the strength of the magnetic fields produced in the heavy-ion collisions¹⁰. Thus, the high-energy Pb–Pb collisions at the LHC provide the best opportunity for producing MMs.

We have considered two approximate approaches to the calculation of the overall MM production cross-section: the free-particle approximation (FPA)²⁷ given by equation (5) and the locally constant field approximation (LCFA)¹⁰ given by equation (4) (Methods). In the FPA, the spacetime dependence of the electromagnetic field of the heavy ions is treated exactly, but MM self-interactions are neglected. Conversely, in the LCFA, the spacetime dependence of the electromagnetic field is neglected but MM self-interactions are treated exactly. In this way the two approximations are complementary, with uncorrelated uncertainties. In addition, for the FPA, the leading effects of MM self-interactions have been shown to enhance the cross-section, and for the LCFA the leading effects of spacetime dependence have also been shown to enhance the cross-section^{10,27}. Thus, while neither approximation provides a complete calculation of the production cross-section, both are expected to yield conservative lower limits. We conservatively use the smaller cross-section in our final MM mass bounds.

To study experimentally the production of MMs created via the Schwinger mechanism in Pb–Pb heavy-ion collisions at the LHC, one also needs to be able to calculate the kinematics of the produced MMs, thus allowing the efficiency of their detection to be assessed. At LHC energies, the expected momentum distribution of MMs is primarily due to the time dependence of the electromagnetic field of the ultrarelativistic heavy ions. The momentum distribution predicted by the LCFA is narrower than what is allowed by the time–energy uncertainty principle, whereas the FPA prediction saturates it²⁷. The failure of the LCFA to yield a consistent momentum distribution is due to the assumption of the instantaneous nature of the production process. In this work, only the FPA is used for the momentum distribution of Schwinger-produced MMs. Nevertheless, the total cross-section in the LCFA still provides important information on the effects of MM self-interactions on the production process. The expression for the FPA momentum distribution is given in equation (6). The uncertainty in the expression is expected to be subdominant compared to that in the total cross-section. Extended Data Fig. 2 shows the transverse momentum distribution for Schwinger MMs derived from the FPA, as a function of MM mass (M) plotted versus MM β , the ratio of velocity to the speed of light in vacuum.

The Monopole and Exotics Detector at the LHC (MoEDAL) is optimized for the detection of MMs and other highly ionizing particles. MoEDAL has reported one of the strongest limits on point-like MM production in proton–proton collisions¹², and has set more recently first limits on the production of dyons (particles with both magnetic and electric charges) in a collider experiment²⁸. Deployed in the LHCb (Large Hadron Collider beauty) experiment’s VELO (Vertex LOcator) cavern around interaction point 8 (IP8), MoEDAL comprises two independent, passive detectors—the magnetic monopole trappers (MMTs) and nuclear track detectors (NTDs). NTDs are made of stacks of thin plastic sheets. When a highly ionizing particle traverses the NTDs, it damages the chemical bonds in the sheets along its path. Etching the NTDs expands the damaged region to the point that it can be detected with an optical microscope, exposing the track of the particle. Owing to their positioning and threshold properties, the NTDs are sensitive only to new physics. Chemical processing, optical microscope scanning and analysis of the NTD data are complicated, time-consuming processes. We plan to release first searches for MM (starting from proton–proton collisions) with NTDs in the near future. The MMTs, used in this work, consist of three components deployed in the front and lateral regions around IP8 at distances

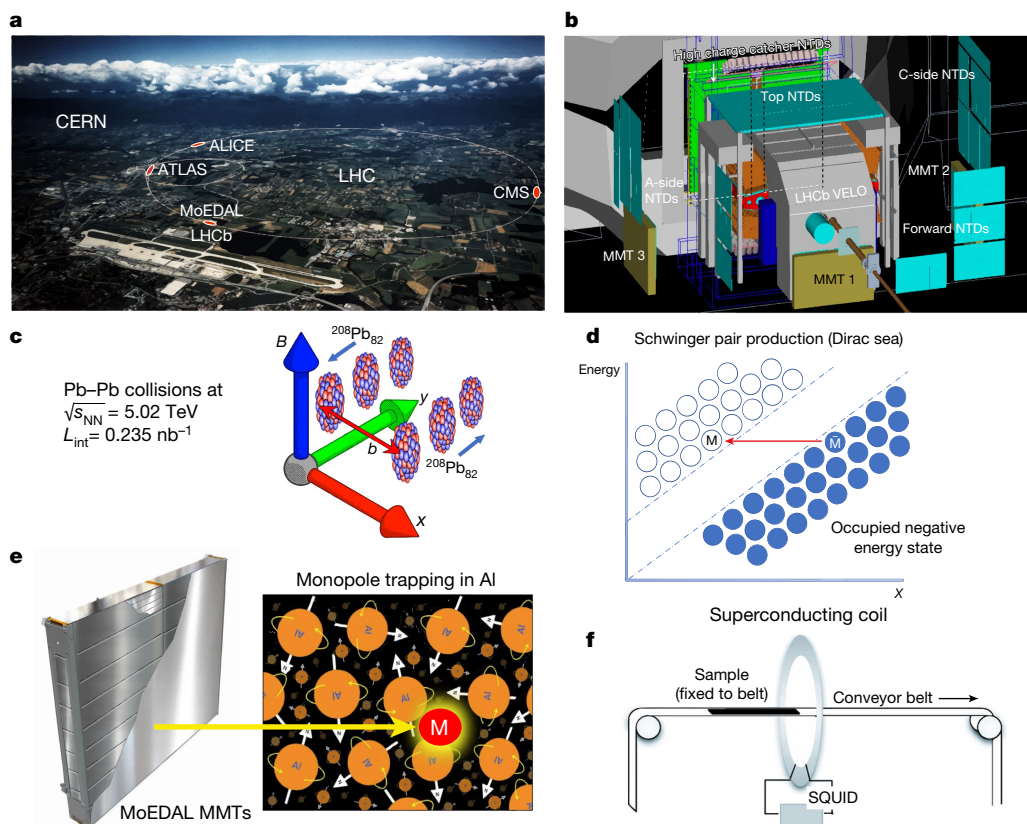


Fig. 1 | Schematic diagram for the search for Schwinger MMs with MoEDAL.

a, The MoEDAL experiment is located at interaction point 8 (IP8) of the LHC. The location of the ALICE, ATLAS and CMS experiments are also indicated. **b**, It has an array of MMT detectors around the interaction point. **c**, Peripheral Pb–Pb heavy-ion collisions produce strong magnetic fields. The 2018 Pb–Pb run with an integrated luminosity at IP8 (L_{IP8}) of 0.235 nb^{-1} . B is the magnetic field of the heavy ions along the y axis, the z axis is the direction of motion of ions, and the x axis is the direction along which the impact parameter b is

measured. **d**, A qualitative sketch describing the Schwinger pair production process in presence of a strong magnetic field from a Dirac sea of negative energy states. A monopole (M) with negative energy tunnels into the positive energy states, leaving behind a positive energy anti-monopole (\bar{M}). **e**, A schematic of one layer of the MMT. After production, an MM may be trapped in an MMT detector. **f**, Samples from the MMTs are passed through a superconducting coil, and the magnetic charge of a trapped MM will induce a signal in a SQUID detector (sensor and electronics).

between 1 and 2 m. Each component is made from 14–18 boxes, with each box made of four layers of 12 aluminum bars. The nominal bar dimensions are $25.4 \times 25.4 \times 190 \text{ mm}$. The total mass of the MMTs used in this study is 880 kg. There is no magnetic field in the region that would affect the MM trajectories. Because of its large anomalous magnetic moment, it is estimated that a ^{27}Al nucleus (100% natural abundance) would bind a magnetically charged particle with an energy of 0.5–2.5 MeV (refs. ^{29–31}). Details of MM binding to matter are discussed in Methods. After exposure, the MMT bars are scanned for trapped magnetic charges with a d.c. SQUID long-core magnetometer (Model 755, 2G Enterprises) installed at the ETH Zurich Laboratory for Natural Magnetism. Fig. 1 shows a schematic diagram of this search.

The mean expected rate of trapped MMs, R_{exp} , is defined as the mean number of MMs expected to be trapped during the Pb–Pb collision run. It is determined using a Monte Carlo simulation that is described further in the Methods section. For each MM mass and magnetic charge considered, the initial momenta are sampled from the Schwinger FPA kinematic distribution. The MMs are then propagated through the realistic geometry of the LHCb and MoEDAL detectors using the Geant4 toolkit³². The MMT trapping efficiency, ϵ , is defined as the ratio of the number of MMs trapped by MMTs to the total number of generated MMs. The trapping condition in the simulation ensures that the energies of the MMs are less than 0.5 MeV. The mean expected rate is calculated for a given mass and magnetic charge as a product of the trapping efficiency, luminosity and production cross-section.

The systematic uncertainty in the expected rate of trapped MMs owing to the finite statistics of the Monte Carlo samples is less than 2% for a magnetic charge of $1g_D$, increasing to 2–7% for $2g_D$, and reaching 20% for $3g_D$ due to the low trapping efficiency. The systematics in the calculation of energy losses by Geant4 are between 1–7% (ref. ³³), and the uncertainty in the luminosity is better than 5%. The dominant systematic uncertainty arises from the efficiency calculation, and is mainly due to the uncertainty in the material budget, which is determined by inspection and direct measurement. The error in the measurements of component materials present in the VELO cavern is estimated by minimal and maximal geometry models, which encompass the uncertainties. Generally, the VELO vacuum vessel is modelled with high precision, whereas the cables and pipes that are downstream of the VELO, as well as the inner regions of the vacuum pump and vacuum manifold, are not as well known. We model the cables and small pipes as a set of vertical stainless steel rods, which represent 2.3% of the radiation length on average. We vary the radius of the rods in the simulation from 0.01 cm (minimal geometry) to 0.5 cm (maximum geometry). We also add a layer of stainless steel to the inner region of the vacuum tank. The default geometry contains 2.64 mm of stainless steel, representing 15% of added radiation length. The minimal geometry contains no extra stainless steel. The maximal geometry, included as a conservative case, consists of 5.28 mm of extra stainless steel, that is, 30% of a radiation length. For magnetic charges larger than $3g_D$ all simulated MMs range out in the default geometry before reaching the MMTs. A more detailed discussion of the uncertainty calculation can be found in Methods.

The MoEDAL detector, consisting of 880 kg of MMTs placed in the forward and lateral regions, was exposed to 0.235 nb^{-1} ($1 \text{ nb} = 1.0 \times 10^{-7} \text{ fm}^2$) of Pb–Pb collisions at $\sqrt{s_{\text{NN}}} = 5.02 \text{ TeV}$ obtained in November 2018. The 0.235 nb^{-1} exposure corresponds to approximately 1.8×10^9 Pb–Pb collisions in total, and approximately 5.9×10^8 of these are ultraperipheral. The much smaller (less than $10 \mu\text{b}^{-1}$) Pb–Pb run in 2016 was not included in the analysis, to ensure uniform beam conditions. The MMTs were scanned using the d.c. SQUID magnetometer for the presence of trapped magnetic charges. No statistically significant signal was observed. The existence of an MM with $|g| \geq 0.5g_{\text{D}}$ in the trapping volume was excluded at more than 3σ .

MMs with masses up to $75 \text{ GeV}/c^2$ to $70 \text{ GeV}/c^2$ for magnetic charges from $1g_{\text{D}}$ to $3g_{\text{D}}$, respectively, are excluded at the 95% confidence level by comparing with the calculated Schwinger production cross-section, as shown in Table 1. The statistical significances of the limits take into account the uncertainty of R_{exp} owing to the systematics, which is dominated by the material budget (see Extended Data Tables 1–5) and Poisson statistics. The expected numbers of events depend exponentially on the MM mass, so even large systematic uncertainties have only a small effect on the mass limits. Details of the measurement, calibration and statistical procedures are provided in Methods. We note that the FPA mass bounds for $|g| \geq 2g_{\text{D}}$ are lower than for $1g_{\text{D}}$, because the increase in the cross-section is offset by the rapid decrease in efficiency for higher magnetic charges. This is not the case for the LCFA, where the cross-section grows for higher magnetic charges faster than the efficiency drops.

Fig. 2a shows the exclusion regions in the magnetic charge versus mass plane for the FPA and LCFA approximations. Our results exclude a much larger region of the parameter space than previous limits from other production channels, including production of MM pairs in heavy-ion collisions at the CERN SPS (Super Proton Synchrotron)³⁴ via a thermalized quark gluon plasma, which was re-interpreted in ref.³⁵ in terms of the Schwinger mechanism. In addition, these limits are model-independent, and thus valid for both elementary and composite MMs. Fig. 2a also reports limits from indirect searches of MMs produced close to the surface of neutron stars, as well as from cosmological reheating and Big Bang nucleosynthesis³⁵.

The main result of this work (Fig. 2a) takes advantage of the recent progress^{10,35} in the calculation of the overall production rate of MMs in strong magnetic fields, which allows one to place limits on MM

Table 1 | 95% confidence level mass limits (in GeV/c^2) on MM pair production in LHC Pb–Pb collisions

Cross-section approximation	Magnetic charge (g_{D})		
	1	2	3
FPA	90	70	70
LCFA	75	210	388
Conservative limit	75	70	70

masses. An alternative way to present the results is to interpret the zero observed rate of MMs as a first experimental constraint on the cross-section for the Schwinger mechanism for MM production, assuming the FPA production kinematics. This approach is complementary and free of potential theoretical prejudice on the overall production rate, relying only on the observed rate, measured luminosity and MM trapping efficiency calculated under the FPA assumption. Fig. 2b shows the 95% exclusion regions on the cross-section for magnetic charges 1, 2 and $3g_{\text{D}}$.

Conclusions

The MoEDAL detector took 0.235 nb^{-1} of data in the Pb–Pb heavy-ion run at $\sqrt{s_{\text{NN}}} = 5.02 \text{ TeV}$, that took place in November 2018, the last year of Run-2 at the LHC. The MMT detectors exposed during this run were scanned for the presence of trapped magnetic charge using the SQUID magnetometer. No signal candidates were observed. This allowed the exclusion of production via the Schwinger mechanism of MMs with Dirac charges $1g_{\text{D}} \leq g \leq 3g_{\text{D}}$ and masses up to $75 \text{ GeV}/c^2$ at the 95% confidence level. This limit from a collider experiment is based on a non-perturbative calculation of the MM production cross-section. In addition, this direct search is sensitive to MMs that are not point-like. The current study constitutes, therefore, a search in which finite-size MMs are potentially detectable, not subject to the exponential suppression of their production cross-section expected in Drell–Yan or photon–fusion production.

In the previous literature, exclusion mass limits spanning the $1,725\text{--}2,370 \text{ GeV}/c^2$ range, with corresponding cross-section limits of the order of femtobarns, were obtained assuming Drell–Yan or photon–fusion production for various spin assumptions and magnetic

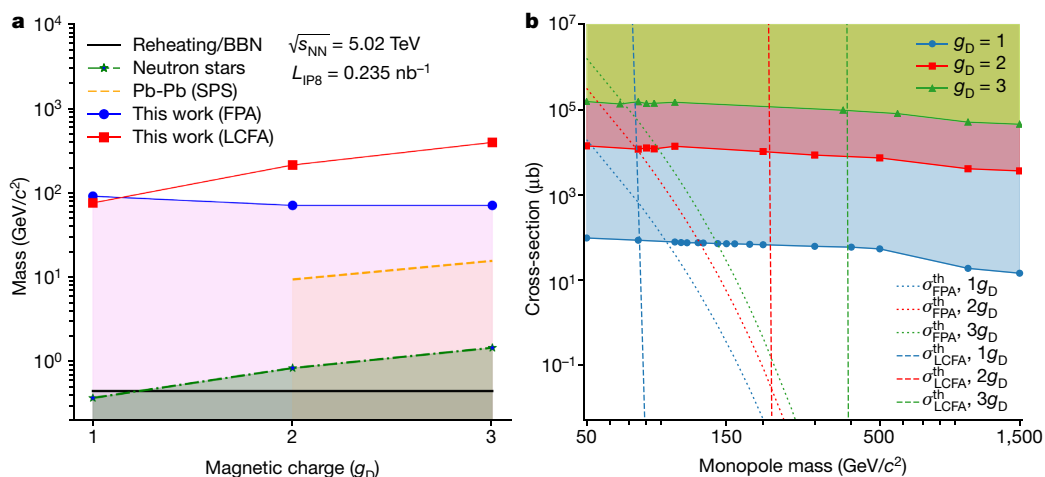


Fig. 2 | 95% confidence level exclusion regions. a, The 95% confidence level mass exclusion regions obtained using the FPA (blue) and LCFA (red) cross-section of MM production via the Schwinger mechanism for Pb–Pb collisions at $\sqrt{s_{\text{NN}}} = 5.02 \text{ TeV}$ and an integrated luminosity at IP8 (L_{IP8}) of 0.235 nb^{-1} , with the conservative exclusion region shaded violet. Limits resulting from other production channels³⁵ are also shown for

comparison. BBN, Big Bang nucleosynthesis. **b**, The 95% confidence level exclusion regions on the cross-section for MM production via the Schwinger mechanism for Pb–Pb collisions at $\sqrt{s_{\text{NN}}} = 5.02 \text{ TeV}$ and an integrated luminosity at IP8 (L_{IP8}) of 0.235 nb^{-1} , as functions of the MM mass for magnetic charges $1g_{\text{D}}$ (blue), $2g_{\text{D}}$ (red) and $3g_{\text{D}}$ (green). The dotted and dashed lines represent the theoretical FPA ($\sigma_{\text{FPA}}^{\text{th}}$) and LCFA cross-sections ($\sigma_{\text{LCFA}}^{\text{th}}$), respectively.

charges up to $5g_D$ (refs. ^{28,36–38}), which constrain light-MM solutions of several theoretical models. The exclusion mass obtained here are below the TeV range (with corresponding cross-section limits of the order of microbarns) because the production cross-section depends exponentially on the MM mass. Nonetheless, the current search is pioneering owing to its use of nonperturbatively calculated cross-sections and is, to the best of our knowledge, the first to have sensitivity to composite MM production at a collider. To ensure the soundness of our lower mass bounds, we have consistently made conservative assumptions. There is substantial scope for future work to improve the accuracy of theoretical calculations, and for future experimental searches at higher energy and luminosity, so as to extend the mass reach. Apart from the heavy-ion collisions, MMs could have been produced via the Schwinger mechanism by primordial magnetic fields, leading to cosmological implications³⁹. The Schwinger production mechanism could also be investigated in proton–proton collisions, where, at higher Lorentz factors, the magnetic field may be stronger than in Pb–Pb collisions. However, because it is also localized in a much smaller volume, it is not clear if the same approach is still valid. The exclusion limits from the current search may guide both theorists and experimentalists in their quest towards understanding the nature of magnetic charge.

Online content

Any methods, additional references, Nature Research reporting summaries, source data, extended data, supplementary information, acknowledgements, peer review information; details of author contributions and competing interests; and statements of data and code availability are available at <https://doi.org/10.1038/s41586-021-04298-1>.

- Schwinger, J. On gauge invariance and vacuum polarization. *Phys. Rev.* **82**, 664–679 (1951).
- Affleck, I. K. & Manton, N. S. Monopole pair production in a magnetic field. *Nucl. Phys. B* **194**, 38–64 (1982).
- Dirac, P. A. M. Quantised singularities in the electromagnetic field. *Proc. R. Soc. London A* **133**, 60–72 (1931).
- 't Hooft, G. Magnetic monopoles in unified gauge theories. *Nucl. Phys. B* **79**, 276–284 (1974).
- Polyakov, A. M. Particle spectrum in quantum field theory. *JETP Lett.* **20**, 194–195 (1974).
- Wen, X.-G. & Witten, E. Electric and magnetic charges in superstring models. *Nucl. Phys. B* **261**, 651–677 (1985).
- Mavromatos, N. E. & Mitsou, V. A. Magnetic monopoles revisited: models and searches at colliders and in the cosmos. *Int. J. Mod. Phys. A* **35**, 2030012 (2020).
- Ho, D. L.-J. & Rajantie, A. Classical production of 't Hooft–Polyakov monopoles from magnetic fields. *Phys. Rev. D* **101**, 055003 (2020).
- Ho, D. L.-J. & Rajantie, A. Instanton solution for Schwinger production of 't Hooft–Polyakov monopoles. *Phys. Rev. D* **103**, 115033 (2021).
- Gould, O., Ho, D. L.-J. & Rajantie, A. Towards Schwinger production of magnetic monopoles in heavy-ion collisions. *Phys. Rev. D* **100**, 015041 (2019).
- Huang, X.-G. Electromagnetic fields and anomalous transports in heavy-ion collisions—a pedagogical review. *Rep. Prog. Phys.* **79**, 076302 (2016).
- MoEDAL Collaboration. Magnetic monopole search with the full MoEDAL trapping detector in 13 TeV *pp* collisions interpreted in photon-fusion and Drell–Yan production. *Phys. Rev. Lett.* **123**, 021802 (2019).
- Guth, A. H. Inflationary universe: a possible solution to the horizon and flatness problems. *Phys. Rev. D* **23**, 347–356 (1981).
- Witten, E. Baryons in the $1/N$ expansion. *Nucl. Phys. B* **160**, 57–115 (1979).
- Drukker, A. K. & Nussinov, S. Monopole pair creation in energetic collisions: is it possible? *Phys. Rev. Lett.* **49**, 102–105 (1982).
- Blagojević, M. & Senjanović, P. The quantum field theory of electric and magnetic charge. *Phys. Rep.* **157**, 233–346 (1988).
- Cho, Y. & Maison, D. Monopole configuration in Weinberg–Salam model. *Phys. Lett. B* **391**, 360–365 (1997).
- Kimm, K., Yoon, J. H. & Cho, Y. M. Finite energy electroweak dyon. *Eur. Phys. J. C* **75**, 67 (2015).

- Ellis, J., Mavromatos, N. E. & You, T. The price of an electroweak monopole. *Phys. Lett. B* **756**, 29–35 (2016).
- Mavromatos, N. E. & Sarkar, S. Magnetic monopoles from global monopoles in the presence of a Kalb–Ramond field. *Phys. Rev. D* **95**, 104025 (2017).
- Arunasalam, S. & Kobakhidze, A. Electroweak monopoles and the electroweak phase transition. *Eur. Phys. J. C* **77**, 444 (2017).
- Mavromatos, N. E. & Sarkar, S. Regularized Kalb–Ramond magnetic monopole with finite energy. *Phys. Rev. D* **97**, 125010 (2018).
- Hung, P. Q. Topologically stable, finite-energy electroweak-scale monopoles. *Nucl. Phys. B* **962**, 115278 (2021).
- Sauter, F. Über das Verhalten eines Elektrons im homogenen elektrischen Feld nach der relativistischen Theorie Diracs. *Z. Phys.* **69**, 742–764 (1931).
- Heisenberg, W. & Euler, H. Consequences of Dirac's theory of positrons. *Z. Phys.* **98**, 714–732 (1936).
- Kaspi, V. M. & Beloborodov, A. M. Magnetars. *Ann. Rev. Astron. Astrophys.* **55**, 261–301 (2017).
- Gould, O., Ho, D. L.-J. & Rajantie, A. Schwinger pair production of magnetic monopoles: momentum distribution for heavy-ion collisions. *Phys. Rev. D* **104**, 015033 (2021).
- MoEDAL Collaboration. First search for dyons with the full MoEDAL trapping detector in 13 TeV *pp* collisions. *Phys. Rev. Lett.* **126**, 071801 (2021).
- Milton, K. A. Theoretical and experimental status of magnetic monopoles. *Rep. Prog. Phys.* **69**, 1637–1711 (2006).
- The MoEDAL Collaboration. The physics programme of the MoEDAL experiment at the LHC. *Int. J. Mod. Phys. A* **29**, 1430050 (2014).
- Gamberg, L., Kalbfleisch, G. R. & Milton, K. A. Direct and indirect searches for low-mass magnetic monopoles. *Found. Phys.* **30**, 543–565 (2000).
- Agostinelli, S. et al. Geant4—a simulation toolkit. *Nucl. Instrum. Meth. A* **506**, 250–303 (2003).
- The MoEDAL Collaboration. Search for magnetic monopoles with the MoEDAL prototype trapping detector in 8 TeV proton–proton collisions at the LHC. *J. High Energy Phys.* **2016**, 67 (2016).
- He, Y. D. Search for a Dirac magnetic monopole in high energy nucleus–nucleus collisions. *Phys. Rev. Lett.* **79**, 3134–3137 (1997).
- Gould, O. & Rajantie, A. Magnetic monopole mass bounds from heavy-ion collisions and neutron stars. *Phys. Rev. Lett.* **119**, 241601 (2017).
- ATLAS Collaboration. Search for magnetic monopoles in $\sqrt{s}=7$ TeV *pp* collisions with the ATLAS detector. *Phys. Rev. Lett.* **109**, 261803 (2012).
- ATLAS Collaboration. Search for magnetic monopoles and stable particles with high electric charges in 8 TeV *pp* collisions with the ATLAS detector. *Phys. Rev. D* **93**, 052009 (2016).
- ATLAS Collaboration. Search for magnetic monopoles and stable high-electric-charge objects in 13 TeV proton–proton collisions with the ATLAS Detector. *Phys. Rev. Lett.* **124**, 031802 (2020).
- Kobayashi, T. Monopole–antimonopole pair production in primordial magnetic fields. *Phys. Rev. D* **104**, 043501 (2021).

Publisher's note Springer Nature remains neutral with regard to jurisdictional claims in published maps and institutional affiliations.

© The Author(s), under exclusive licence to Springer Nature Limited 2022

¹Theoretical Particle Physics & Cosmology Group, Physics Department, King's College London, London, UK. ²EAP, Czech Technical University in Prague, Prague, Czech Republic. ³INFN, Section of Bologna, Bologna, Italy. ⁴School of Physics and Astronomy, Queen Mary University of London, London, UK. ⁵Institute of Space Science, Măgurele, Romania. ⁶Experimental Physics Department, CERN, Geneva, Switzerland. ⁷Center for Quantum Spacetime, Sogang University, Seoul, Korea. ⁸Physics Department, University of Alberta, Edmonton, Alberta, Canada. ⁹Theoretical Physics Department, CERN, Geneva, Switzerland. ¹⁰Department of Physics, Concordia University, Montreal, Quebec, Canada. ¹¹University of Nottingham, Nottingham, UK. ¹²Helsinki Institute of Physics, University of Helsinki, Helsinki, Finland. ¹³Department of Earth Sciences, Swiss Federal Institute of Technology, Zurich, Switzerland. ¹⁴Department of Physics, Imperial College London, London, UK. ¹⁵Department of Physics, University of Virginia, Charlottesville, VA, USA. ¹⁶Département de Physique Nucléaire et Corpusculaire, Université de Genève, Geneva, Switzerland. ¹⁷Département de Physique, Université de Montréal, Montreal, Quebec, Canada. ¹⁸Department of Physics and Astronomy, University of Bologna, Bologna, Italy. ¹⁹IFIC, Universitat de València, CSIC, Valencia, Spain. ²⁰Department of Physics and Astronomy, University of Alabama, Tuscaloosa, AL, USA. ²¹Institute for Research in Schools, Canterbury, UK. ²²Department of Physics, University of British Columbia, Vancouver, British Columbia, Canada. ²³Department of Physics and Astronomy, Tufts University, Medford, MA, USA. ²⁴CNAF, INFN, Bologna, Italy. ²⁵Deceased: P. Mermod. ²⁶e-mail: iostrovskiy@ua.edu

Monte Carlo simulation of the MoEDAL experiment

The MM simulation code is developed in Gauss⁴⁰, which is the LHCb simulation framework that uses Geant4 as the simulation engine. MoEDAL simulations use a dedicated Geant4 class that describes production and propagation of MMs⁴¹. The MM ionization energy losses, geometry and material content of the MoEDAL detector and its vicinity are modeled in the simulation. The MMTs are described in Geant4 as sensitive detectors and produce hits when MMs are trapped in them. These hits are recorded in simulation and analysed for calculating efficiency and the expected rate of MMs detection. A custom-made momentum distribution of MMs derived from Schwinger kinematics (equation (3)) is implemented and propagated through the MoEDAL geometry.

Cross-section calculation

In our analysis, the electromagnetic fields are approximated as coherent, classical, event-averaged fields sourced by the heavy ions^{42,43}. In this approximation the fields are determined by integrating the Liénard–Wiechert potentials over the charge distribution of the ions, which is modelled as a Woods–Saxon distribution with radius $R_{\text{pb}} = 6.62$ fm and surface thickness $a_{\text{pb}} = 0.546$ fm^{44,45}. Note that the inclusion of event-by-event fluctuations⁴⁶ can be expected to greatly enhance the overall MM yield, owing to the exponential form of the cross-sections, shown below. We leave this effect as a promising avenue for future work.

In the near vicinity of the collision center, the magnetic field is the largest component of the electromagnetic field, and it points perpendicularly to both the beam axis and the impact parameter, as defined in Fig. 1c. The electric field cancels at the collision centre but in the near vicinity it has a nonzero component parallel to the impact parameter; see ref. ¹¹ for a review.

Following ref. ¹⁰, we calculate the electromagnetic fields on a lattice of points in the vicinity of the collision centre, that is, for x, y, z and ct of order R/γ , where γ is the Lorentz factor at collision. We then perform a fit of the following form to the results:

$$B_y = \frac{B/2}{[1 + \omega^2(t-z)^2]^{3/2}} + \frac{B/2}{[1 + \omega^2(t+z)^2]^{3/2}},$$

$$E_x = \frac{B/2}{[1 + \omega^2(t-z)^2]^{3/2}} - \frac{B/2}{[1 + \omega^2(t+z)^2]^{3/2}}.$$

This model correctly describes the asymptotic behaviour of the electromagnetic fields in ultrarelativistic heavy-ion collisions. It depends on two fit parameters, B and ω , and agrees with direct numerical integration to within ten percent accuracy at all points studied.

For lead-ion collisions at $\sqrt{s_{\text{NN}}} = 5.02$ TeV, we find the peak magnetic field strength occurs for $b = b_{\text{max}} \approx 1.94R_{\text{pb}}$. It takes the value $B = 7.6 \pm 0.3$ GeV², from which the field decays with inverse decay time $\omega = 73 \pm 3$ GeV, where we have used natural units, $c = \hbar = \epsilon_0 = 1$. The uncertainty quoted on these values reflects the stability of the fit results with respect to the underlying assumptions of the fit model. In particular, by minimizing the sum of absolute squared deviations, good agreement can be obtained between the data and the fit in the region around the origin, where the magnetic field is largest. On the other hand, minimizing the sum of relative (that is, fractional) squared deviations gives better agreement for the asymptotic tails. Since we do not know which aspects of the electromagnetic field are most important for MM pair production, we take the differences between the fits as a measure of the uncertainty and assume a uniform distribution within this range. The magnitude of the peak magnetic field is in good agreement with ref. ⁴⁶, in which a Glauber-model Monte Carlo was used to model event-by-event fluctuations and nucleon collisions, finding peak magnetic field strengths of $\langle B_y \rangle \approx 7.0$ GeV² and $\langle |B_y| \rangle \approx 7.5$ GeV² when extrapolated to $\sqrt{s_{\text{NN}}} = 5.02$ TeV. For comparison, we have also computed the

electromagnetic fields using the model of ref. ⁴², yielding $B \approx 9$ GeV² and $\omega \approx 80$ GeV. However, the larger field strengths in this case can be traced back to the unphysical nature of assuming a uniform charge density in a two dimensional disc. We therefore use the more realistic Woods–Saxon charge distribution model in preference.

The MM production cross-section due to the electromagnetic fields present in heavy-ion collisions has been calculated in refs. ^{10,27}. In these works, the authors included only the electromagnetic field due to the non-colliding (spectator) nucleons, and neglected the field due to the colliding (participant) nucleons. This approximation is justified for impact parameters greater than approximately twice the nuclear radius, that is, ultraperipheral collisions⁴⁷. It may also be justified for somewhat less peripheral collision, especially for the early times in which the magnetic field is strongest⁴³. As we will see below, ultraperipheral collisions are expected to yield the greatest MM production cross-sections. In light of this, and of the theoretical uncertainty in the MM production cross-section for smaller impact parameters, we will conservatively include only MM production from ultraperipheral collisions in our analysis. We leave the analysis of more central events, and of the effect of nucleon collisions on MM production, for future work.

In ref. ¹⁰, the MM production cross-section for fixed impact parameter b was calculated in the LCFA and FPA approximations,

$$\frac{1}{2\pi b} \frac{d\sigma_{\text{LCFA}}}{db} \approx \frac{[gB(b)]^4}{18\pi^3 M^4 \omega^2(b) \Omega^2(b)} \exp\left(-\frac{\pi M^2}{gB(b)} + \frac{g^2}{4}\right), \quad (2)$$

$$\frac{1}{2\pi b} \frac{d\sigma_{\text{FPA}}}{db} \approx \frac{[gB(b)]^4}{18\pi^3 M^4 \omega^2(b) \Omega^2(b)} \exp\left(-\frac{4M}{\omega(b)}\right), \quad (3)$$

where $\Omega^2(b) \approx 2/(bR_{\text{pb}})$ is the product of the slow inverse decay lengths of the field perpendicular to the beam axis and M is the MM mass. Both equations were derived for scalar (spin $s = 0$) MMs. Within the LCFA one can demonstrate that the effect of MM spin on the production cross-section is simply a multiplicative factor of $(2s + 1)^{2,48,49}$; however, we will conservatively neglect this factor. Within each of these approximations, equations (2) and (3) are accurate up to a multiplicative $O(1)$ factor. This uncertainty in the pre-exponential factor stems from the approximate evaluation of a functional determinant, discussed further around equation 39 of ref. ¹⁰. It should have only a small effect on our final MM mass bounds, owing to the strong (exponential) dependence of the cross-sections on the MM mass. For the same reason, its effect is subdominant to the uncertainty in B and ω , which enter the exponent.

The total cross-section in the LCFA is strongly dominated by impact parameters in the vicinity of $b = b_{\text{max}} \approx 2R_{\text{pb}}$, at which the magnetic field is maximal. As a consequence, integration over the impact parameter can be carried out using Laplace's method, yielding

$$\sigma_{\text{LCFA}} \approx \frac{2(gB)^{9/2} R_{\text{pb}}^4}{9\pi^2 M^3 \omega^2} \exp\left(-\frac{\pi M^2}{gB} + \frac{g^2}{4}\right), \quad (4)$$

where all parameters are evaluated at $b = b_{\text{max}}$. For the MM masses we have studied, the range of impact parameters that contribute strongly to the total cross-section deviates from b_{max} by less than about 1%.

The total cross-section in the FPA is also dominated by impact parameters in the vicinity of b_{max} , though less strongly so. The integration over impact parameters yields

$$\sigma_{\text{FPA}} \approx \left[\frac{\omega}{M} + c_{\text{central}} \right] \frac{2(gB)^4 R_{\text{pb}}^4}{9\pi^2 M^4 \omega^2} \exp\left(-\frac{4M}{\omega}\right), \quad (5)$$

where all parameters are evaluated at $b = b_{\text{max}}$. In this expression, the first term inside the square brackets arises from the contribution due to ultraperipheral collisions, with $b \geq b_{\text{max}}$, and the second term $c_{\text{central}} > 0$ arises from integration over the contribution due to more

central collisions with $b < b_{\max}$. The condition $b < b_{\max}$ corresponds to events in centrality classes 0–68%^{44,45}.

Ignoring the effect of the nucleon collisions on the production process would result in $c_{\text{central}} \approx 2/7$, in which case these more central collisions would account for 20–30% of the total cross-section for the range of masses we have studied within the FPA. However, the effects of nucleon collisions could substantially modify the production cross-section for these more central collisions, and were not accounted for in the derivation of equation (3)¹⁰. To avoid this uncertainty in our FPA analysis, we exclude all MM production from impact parameters $b < b_{\max}$, in which there are a sizeable number of nucleon collisions. This amounts to making the conservative choice $c_{\text{central}} = 0$ in equation (5).

Note that at LHC energies Schwinger production of MMs would occur well before the thermalization of the quark–gluon plasma. This is because the magnetic field decays on a timescale of order $1/\omega$, shorter by around two orders of magnitude than the thermalization time of the quark–gluon plasma⁵⁰. Thus, while the development of conductivity in the quark–gluon plasma remains an important source of uncertainty for predictions of the chiral magnetic effect^{51,52}, it is not expected to be relevant for Schwinger production of MMs.

Both the FPA and the LCFA are semiclassical approximations, yielding exponential forms for the cross-section. Consequently, the expressions are quantitatively reliable only when the exponent is negative and has magnitude greater than one. Outside this range, the semiclassical analysis indicates that there is no exponential suppression for MM production. For sufficiently light MMs, the magnitude of the exponent is less than one, indicating the breakdown of the semiclassical approximation and consequently unsuppressed MM production. In the FPA this occurs for $M \lesssim \omega/4 \approx 18$ GeV and in the LCFA this occurs for $M \lesssim \sqrt{g^3 B/4\pi} \approx 73(g/g_D)^{3/2}$ GeV. For such light MMs, we assume the production cross-section to be at least as large as that for heavier monopoles in which there is exponential suppression.

For the distribution of momentum \mathbf{p} we use the following result, based on a calculation within the FPA, for the relative probability²⁷

$$\frac{d\sigma_{\text{FPA}}(\mathbf{p})}{d\mathbf{p}} / \frac{d\sigma_{\text{FPA}}(0)}{d\mathbf{p}} = \exp \left[-\frac{4}{\omega} \left(\sqrt{M^2 + |\mathbf{p}|^2} - M \right) \right]. \quad (6)$$

This equation describes an isotropic momentum distribution. Within the FPA, there is a residual $O(1)$ uncertainty regarding the p_z dependence, which is not fully accounted for by this expression, and which is discussed at length in ref. ²⁷. In short, the true momentum distribution in the FPA is expected to differ from equation (6) by a moderate anisotropy along the beam axis, though its precise form is unknown. This uncertainty in the momentum distribution will result in an $O(1)$ uncertainty in the final efficiency, which is subdominant compared to the uncertainty in the total cross-section.

Efficiency calculation

The trapping efficiency, shown in Extended Data Tables 1–5, depends on the kinematics predicted by the MM model, the MM mass and magnetic charge, the material traversed by the MMs, and the corresponding energy losses. The efficiency is negligible for MMs with very low momentum, as slow-moving MMs would lose their energy through ionization before reaching the detectors. The efficiency increases almost linearly with increase in momentum until the MMs become energetic enough to pass through the MMTs without getting trapped. The efficiency then decreases with momentum above a threshold value that depends on the MM mass and magnetic charge. The Bethe–Bloch equation modified for MMs with magnetic charge $g = ng_D$ ($n = 1, 2, 3, \dots$) that describes the ionization energy losses is given by:

$$\frac{dE}{dx} = \frac{4\pi e^2 g^2}{m_e c^2} n_e \left[\ln \frac{2m_e c^2 \beta^2 \gamma^2}{I_m} - \frac{1}{2} + \frac{K(|g|)}{2} - B(|g|) - \frac{\delta}{2} \right], \quad (7)$$

where n_e is the number of electrons per unit volume in the medium, I_m is the mean ionization potential of the crossed medium, m_e is the electron mass, γ is the Lorentz factor, δ is the density effect correction, $K(|g|) = (0.406; 0.346$ if $g > 1g_D$) is the QED correction and $B(|g|) = 0.248, 0.672, 1.022, 1.243, 1.464$ is the Bloch correction for $g = 1g_D, \dots, 5g_D$, respectively⁵³. Therefore, MMs with higher magnetic charges ($|g| > 1g_D$) are expected to have greater ionization losses and, as a consequence, tend to range out before reaching the MMTs, predominantly stopping in the upstream material. Also, keeping other parameters unchanged, MMs with lower masses have a higher velocity, leading to greater energy losses, and hence failure to reach the MMTs. The size of trapping efficiency decreases sharply for $>1g_D$ magnetic charges. For $1g_D$, ϵ varies between 1.1 – 1.5×10^{-4} for MM mass 50–105 GeV. For $2g_D$, ϵ varies between 3.3 – 4.4×10^{-7} for MM mass 50–85 GeV.

Uncertainties and statistical methods

The mean Poisson rate, R_{exp} , gives the expected number of MMs trapped in the MMTs during the MoEDAL Pb–Pb data-taking run. It is calculated as the product of the MM cross-section, the luminosity (exposure), and the trapping efficiency. We exclude MM masses with non-zero expected events, based on the non-observation of MM after scanning the MMTs. The confidence level of exclusion (CL_{exc}) is determined from the Poisson statistics on R_{exp} , Monte Carlo statistical errors, and systematic uncertainties on the detector geometry, cross-section (due to B and ω uncertainties), energy losses, and magnetometer response (false negatives, discussed in the following section). The Monte Carlo statistical uncertainties are confined to less than 2% (7%) for $1g_D$ ($2g_D$), owing to the large Monte Carlo samples generated ($\sim 5 \times 10^7$ – 1×10^{10} , depending on the MM mass and magnetic charge) but increase to $\sim 20\%$ for $3g_D$ owing to the low trapping efficiency ($\sim 2.3 \times 10^{-9}$). The false negative probability of the magnetometer response is 0.2% (ref. ¹²) for magnetic charges $g > g_D$ and decreases with increasing magnetic charge. The dE/dx calculation results in a relative uncertainty in the range 1–7%³³. The uncertainty of B and ω is specified in an earlier section. The remaining, dominant source of uncertainty is due to the material budget, described in the main text.

Extended Data Fig. 1 shows an example of the dependence of the mean rate on the MM mass. The rate is calculated for the FPA cross-section, which gives the conservative limits used in the main text. Extended Data Tables 1–5 show the efficiency and expected rate of trapped MMs produced by the Schwinger mechanism for different values of the MM mass and magnetic charge. Cross-section values are also shown, with a spread corresponding to B and ω uncertainties. The spread in efficiency is between the maximal and minimal geometry models. We note that, although the resulting spread of R_{exp} is large, its impact on the mass limits is strongly suppressed, owing to the exponential dependence of the cross-section on the MM mass.

The efficiency and cross-section uncertainties lead to a systematic spread in R_{exp} . The probability to observe no MMs in the scanned MMTs given the range of R_{exp} , $P(0 | (R_{\text{exp}}^{\min}, R_{\text{exp}}^{\max}))$, is calculated using the toy Monte Carlo approach. A uniform probability distribution for the range of possible efficiency values is assumed, reflecting no preference between the minimal and maximal geometry models. For $g = 3g_D$, the range's left boundary is the upper limit on the efficiency for the maximal geometry. Likewise, a uniform distribution is assumed for the B and ω variables, which are expected to be 100% positively correlated. A toy value of the expected rate R_{exp}^i is calculated using efficiency and cross-section values on the basis of random draws from their distributions. Then, a toy observed rate R^i is randomly drawn from a Poisson distribution with $\mu = R_{\text{exp}}^i$. The process is repeated 10^5 times. The probability $P(0 | (R_{\text{exp}}^{\min}, R_{\text{exp}}^{\max}))$ is then defined as the fraction of $R^i = 0$ entries in the toy R^i distribution. Finally, the CL_{exc} is calculated as $(1 - P(0 | (R_{\text{exp}}^{\min}, R_{\text{exp}}^{\max}))) \times 100\%$.

To test the robustness of this approach against the choice of the distribution of the efficiency, ϵ , additional choices are considered. In the first test, a Gaussian distribution with $\mu = (\epsilon_{\max} + \epsilon_{\min})/2$ and $\sigma = (\mu - \epsilon_{\min})/2$,

truncated at ϵ_{\min} and ϵ_{\max} , is assumed. In the second test, a skewed Gaussian distribution centered at ϵ corresponding to the default geometry, with $\sigma = (\mu - \epsilon_{\min})/2$ and skewness parameter set to 1 or 2, is assumed. The choice of a Gaussian distribution reflects our expectation that the default geometry is the most likely one. The direction of the skewness is dictated by the fact that the efficiency changes more rapidly when the material is removed from the geometry, compared to when it is added. In all considered cases the resulting CL_{exc} agrees with or is slightly stronger than that for the uniform distribution of ϵ . Additionally, for $g = 3g_D$, the calculation was repeated using uniform distribution with the maximal geometry's efficiency assumed to be two orders of magnitude lower than the limit obtained with the finite Monte Carlo statistics (Extended Data Tables 3–5). The mass limit decreases by $\sim 5 \text{ GeV}/c^2$.

Magnetometer measurements

The SQUID magnetometer uses the induction technique⁵⁴ that is directly sensitive to the presence of an isolated magnetic charge, which would excite a persistent current in the device. The expected response of a SQUID magnetometer needs to be quantified before such a current is measured. The magnetometer setup consists of a flux measuring system with two pick-up coils of diameter 8 cm along its longitudinal axis. The transportation of samples takes place via an access shaft with diameter 4 cm. A more detailed description is provided in ref.⁵⁵.

The bars of the MoEDAL MMTs were scanned for the presence of magnetic charges with a d.c. SQUID long-core magnetometer. Each sample was scanned through the superconducting coil at least twice, and the magnetometer's response was recorded before, during and after each passage. The current induced in the superconducting coil is directly proportional to the difference in magnetic flux in the direction of transport. The magnetometer feedback, after multiplication by a calibration constant C is converted into a magnetic pole strength S (in units of g_D). Two independent methods, the solenoid method and the convolution method, were used to perform calibration of the instrument⁵⁵. The solenoid method used long, thin solenoids that mimic an MM of well known magnetic charge. The magnetometer response was measured to be linear and charge symmetric in a range corresponding to 0.1–300 g_D (ref.³³). A magnetic charge present in the sample would induce a persistent current in the superconducting coil, proportional to its pole strength. The difference between the measured induced currents before (I_1) and after (I_2) passage of the sample, while simultaneously adjusting for corresponding contributions (I_1^{tray} and I_2^{tray}) of the empty conveyer tray, is defined as the persistent current. We calculate the magnetic pole strength as

$$S = C[(I_2 - I_1) - (I_2^{\text{tray}} - I_1^{\text{tray}})].$$

For a dipole, the currents induced by the north and south pole in a sample cancel out. The current expected from a Dirac MM was emulated using a long solenoid. An MM present in the sample would record a persistent current significantly different from zero. After passing through the superconducting coil, a sample was considered an MM candidate whenever the measured pole strength diverged from zero by more than $0.4g_D$. The candidates were scanned four or five times each. A sample with an actual magnetic charge would yield the same persistent current in repeated measurements. However, after multiple measurements on samples, whenever the first one diverged from zero, subsequent measurements were consistent with zero. The measured outliers could be attributed to spurious flux jumps occurring as a result of ferromagnetic impurities in the sample, noise currents in the superconducting loop, variations in external magnetic fields, and other known instrumental and environmental factors³³. The probability that a sample containing an MM with $|g| \geq 0.5g_D$ would repeatedly yield a persistent current lower than the detection threshold is estimated by the rate of spurious jumps between $0.25g_D$ and $0.5g_D$. This false negative probability is calculated at $0.2\%^{12}$. For MMs with charges larger than $0.5g_D$, this number is even

smaller. This calculation does not depend on the structure or the mass of the magnetic charge. Thus, the presence of an MM with $|g| \geq 0.5g_D$ was excluded in all samples at more than 3 sigma. After scanning, the bars are returned to CERN for storage and further use.

Monopole binding to matter

An early investigation⁵⁶ of charged particles of arbitrary magnetic moment moving in the field of the MM with an external electric field concluded that the MM can couple to matter with chemical-bond-level energies. Additionally, a number of authors have predicted that nucleons, nuclei, atoms and even molecules, will bind to slow-moving monopoles via the interaction of the monopole with the magnetic moments of these systems^{31,57–64}. It has been suggested that an atomic bound state will have such a long lifetime that it is practically stable^{63,64}. However, it has also been predicted that a bound state of an atom with an MM will rapidly contract to a state where the monopole binds directly to an atomic nucleus or a nucleon^{31,57–62}.

It seems certain that MMs will bind to all nuclei because the extremely strong magnetic field in their vicinity will disrupt the nucleus and bind to the nuclear, or even the subnuclear, constituents³¹. The possibility has been discussed that such a slow-moving or trapped MM could create a kind of metastable nuclear state that could spontaneously fission^{65,66}. This is due to the weakening of the Coulomb barrier inhibiting the fission by the magnetic interaction of the MM, which has a longer range than the nuclear force. Such effects are highly model-dependent and difficult to estimate. The MoEDAL trapping detector consists of over 99.9% ²⁷Al. If an MM bound to the aluminium lattice can induce the fission of the stable ²⁷Al in which it is bound, the 'freed' MM would then bind to resulting fragments or eventually to a nucleon. There is also the possibility that an MM would bind to an atom and not a nucleus. Additionally, an MM that binds to a proton would pick up an electron to create a monopole atom⁶¹. Thus, even if the stopping, or bound, MM did cause the fission of nuclei in the vicinity, it would still not invalidate the statement that they are ultimately captured in the MoEDAL trapping volume.

For the MM to be detectable using the MoEDAL MMT, the bound complex of nucleus, nucleon, or atom and MM must be strongly attached to the crystalline lattice of the material. Presumably, any bound state with an atom in the lattice would necessarily be bound. The lifetime of a monopole nucleus or nucleon bound state can be estimated by considering simple tunnelling, where the decay rate can be estimated using the Wentzel–Kramers–Brillouin (WKB) formula. Previous work³¹ has shown that even for aluminium trapping volumes placed in a magnetic field of 1.5 T, with a magnetic charge number of one, we only need a binding energy of the order of 1 eV to get a 10-year lifetime. In fact, the calculated binding energy is of the order of 0.5–2.5 MeV^{29–31}. It would take a major disruption of the lattice to dislodge a trapped monopole state, arising from large (kV) electric fields or multi-T magnetic fields. Neither of these are present at the MoEDAL intersection region, where the only magnetic fields are due to the Earth and the small fringe fields from the LHCb dipole magnet, which are less than $\sim 10 \text{ mT}$.

Data availability

All data used to produce the results of this work, along with the data points shown in the main figures of the paper are stored either on CERN lplus server or on CERN's GitLab. They are available upon request to the corresponding author without specific conditions. Source data are provided with this paper.

Code availability

All code used to produce the results of this work, including code to perform statistical analysis and produce the figures, is stored on CERN's GitLab server and is available upon request to the corresponding author without specific conditions.

40. Clemencic, M. et al. The LHCb simulation application, Gauss: design, evolution and experience. *J. Phys. Conf. Ser.* **331**, 032023 (2011).
41. King, M. Simulation of the MoEDAL experiment. *Nucl. Part. Phys. Proc.* **273–275**, 2560–2562 (2016).
42. Kharzeev, D. E., McLerran, L. D. & Warringa, H. J. The effects of topological charge change in heavy ion collisions: “event by event P and CP violation”. *Nucl. Phys. A* **803**, 227–253 (2008).
43. Gursoy, U., Kharzeev, D. & Rajagopal, K. Magnetohydrodynamics, charged currents and directed flow in heavy ion collisions. *Phys. Rev. C* **89**, 054905 (2014).
44. ALICE Collaboration. Centrality determination of Pb–Pb collisions at $\sqrt{s_{NN}} = 2.76$ TeV with ALICE. *Phys. Rev. C* **88**, 044909 (2013).
45. ALICE Collaboration. Centrality dependence of particle production in p –Pb collisions at $\sqrt{s_{NN}} = 5.02$ TeV. *Phys. Rev. C* **91**, 064905 (2015).
46. Deng, W.-T. & Huang, X.-G. Event-by-event generation of electromagnetic fields in heavy-ion collisions. *Phys. Rev. C* **85**, 044907 (2012).
47. Baltz, A. J. The physics of ultraperipheral collisions at the LHC. *Phys. Rep.* **458**, 1–171 (2008).
48. Kruglov, S. I. Pair production and vacuum polarization of vector particles with electric dipole moments and anomalous magnetic moments. *Eur. Phys. J. C* **22**, 89–98 (2001).
49. Gould, O. & Rajantie, A. Thermal Schwinger pair production at arbitrary coupling. *Phys. Rev. D* **96**, 076002 (2017).
50. Wolschin, G. Aspects of relativistic heavy-ion collisions. *Universe* **6**, 61 (2020).
51. Tuchin, K. Time and space dependence of the electromagnetic field in relativistic heavy-ion collisions. *Phys. Rev. C* **88**, 024911 (2013).
52. Inghirami, G. et al. Magnetic fields in heavy ion collisions: flow and charge transport. *Eur. Phys. J. C* **80**, 293 (2020).
53. Cecchini, S., Patrizii, L., Sahnoun, Z., Sirri, G. & Togo, V. Energy losses of magnetic monopoles in aluminum, iron and copper. Preprint at <https://arxiv.org/abs/1606.01220> (2016).
54. Alvarez, L. W. et al. A magnetic monopole detector utilizing superconducting elements. *Rev. Sci. Instrum.* **42**, 326–330 (1971).
55. De Roeck, A. et al. Development of a magnetometer-based search strategy for stopped monopoles at the large hadron collider. *Eur. Phys. J. C* **72**, 2212 (2012).
56. Malkus, W. V. R. The interaction of the Dirac magnetic monopole with matter. *Phys. Rev.* **83**, 899–905 (1951).
57. Bracci, L. & Fiorentini, G. Binding of magnetic monopoles and atomic nuclei. *Phys. Lett. B* **124**, 493–496 (1983).
58. Bracci, L. & Fiorentini, G. Interactions of magnetic monopoles with nuclei and atoms: formation of bound states and phenomenological consequences. *Nucl. Phys. B* **232**, 236–262 (1984).
59. Bracci, L. & Fiorentini, G. On the capture of protons by magnetic monopoles. *Nucl. Phys. B* **249**, 519–532 (1985).
60. Olaussen, K. & Sollie, R. Form factor effects on nucleus–magnetic monopole binding. *Nucl. Phys. B* **255**, 465–479 (1985).
61. Olaussen, K., Olsen, H. A., Osland, P. & Øverbø, I. Proton capture by magnetic monopoles. *Phys. Rev. Lett.* **52**, 325–328 (1984).
62. Goebel, C. Binding of monopole to nuclei. In *Monopole '83* (ed. Stone, J. L.) 333–337 (Plenum, 1984).
63. Ruijgrok, Th. W., Tjon, J. A. & Wu, T. T. Monopole chemistry. *Phys. Lett. B* **129**, 209–212 (1983).
64. Ruijgrok, T. Binding of matter to a magnetic monopole. *Acta Phys. Pol. B* **15**, 305–314 (1983).
65. Lipkin, H. J. Effects of magnetic monopoles on nuclear wave functions and possible catalysis of nuclear beta decay and spontaneous fission. *Phys. Lett. B* **133**, 347–350 (1983).
66. Lipkin, H. J. Monopole nucleosynthesis — the wonderful things that monopoles can do to nuclei if they are there. In *Monopole '83* (ed. Stone, J. L.) 347–358 (Plenum, 1984).

Acknowledgements We thank CERN for the LHC’s successful Run-2 operation, as well as the support staff from our institutions without whom MoEDAL could not be operated. We acknowledge the invaluable assistance of particular members of the LHCb Collaboration: G. Wilkinson, R. Lindner, E. Thomas and G. Corti. Computing support was provided by the GridPP Collaboration, in particular by the Queen Mary University of London and Liverpool grid sites. This work was supported by grant PP00P2 150583 of the Swiss NSF; by the UK Science and Technology Facilities Council via the grants ST/L000326/1, ST/L00044X/1, ST/N00101X/1, ST/P000258/1, ST/P000762/1, ST/T000732/1, ST/T000759/1 and ST/T000791/1; by the Generalitat Valenciana via a special grant for MoEDAL and via the projects PROMETEO-II/2017/033 and PROMETEO/2019/087; by MCIU/AEI/FEDER, UE via the grants FPA2016-77177-C2-1-P, FPA2017-85985-P, FPA2017-84543-P and PGC2018-094856-B-I00; by the Physics Department of King’s College London; by NSERC via a project grant; by the V-P Research of the University of Alberta (UofA); by the Provost of the UofA; by UEFISCDI (Romania); by the INFN (Italy); by the Estonian Research Council via a Mobilitas Plus grant MOBTT5; by the Research Funds of the University of Helsinki; and by the NSF grant 2011214 to the University of Alabama MoEDAL group. A.R. was also supported by Institute for Particle Physics Phenomenology Associateship.

Author contributions The Monopole and Exotics Detector at the LHC was constructed and is maintained by the MoEDAL collaboration. A large number of authors contributed to the data processing, detector calibration and Monte Carlo simulations used in this work. The MoEDAL collaboration acknowledges the substantial contributions to this manuscript from A.U. and I.O. (simulation, statistical analysis, result plots, paper writing); O.G., D.L.-J.H. and A.R. (theoretical calculations, paper writing); and N.E.M. and J.P. (paper writing). The manuscript was reviewed and edited by the collaboration and all authors approved the final version of the manuscript.

Competing interests The authors declare no competing interests.

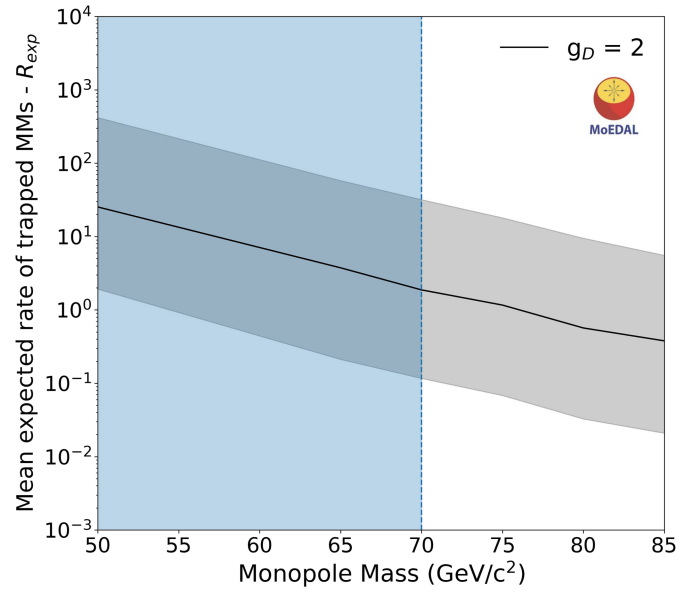
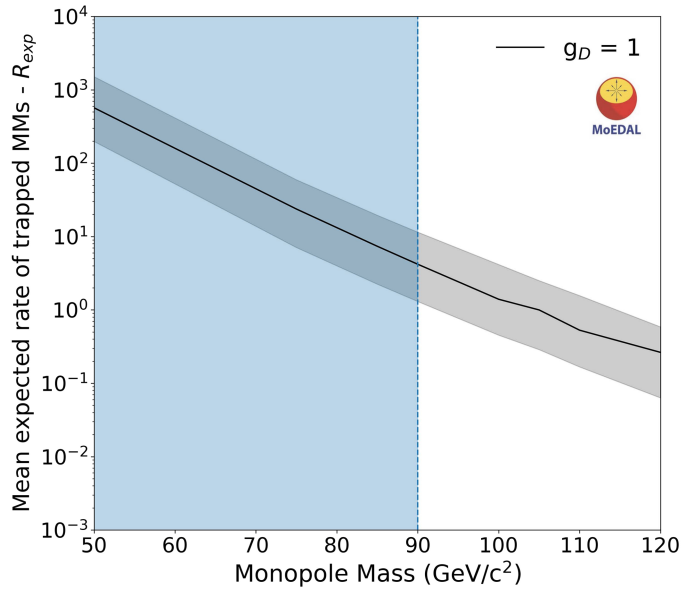
Additional information

Supplementary information The online version contains supplementary material available at <https://doi.org/10.1038/s41586-021-04298-1>.

Correspondence and requests for materials should be addressed to I. Ostrovskiy.

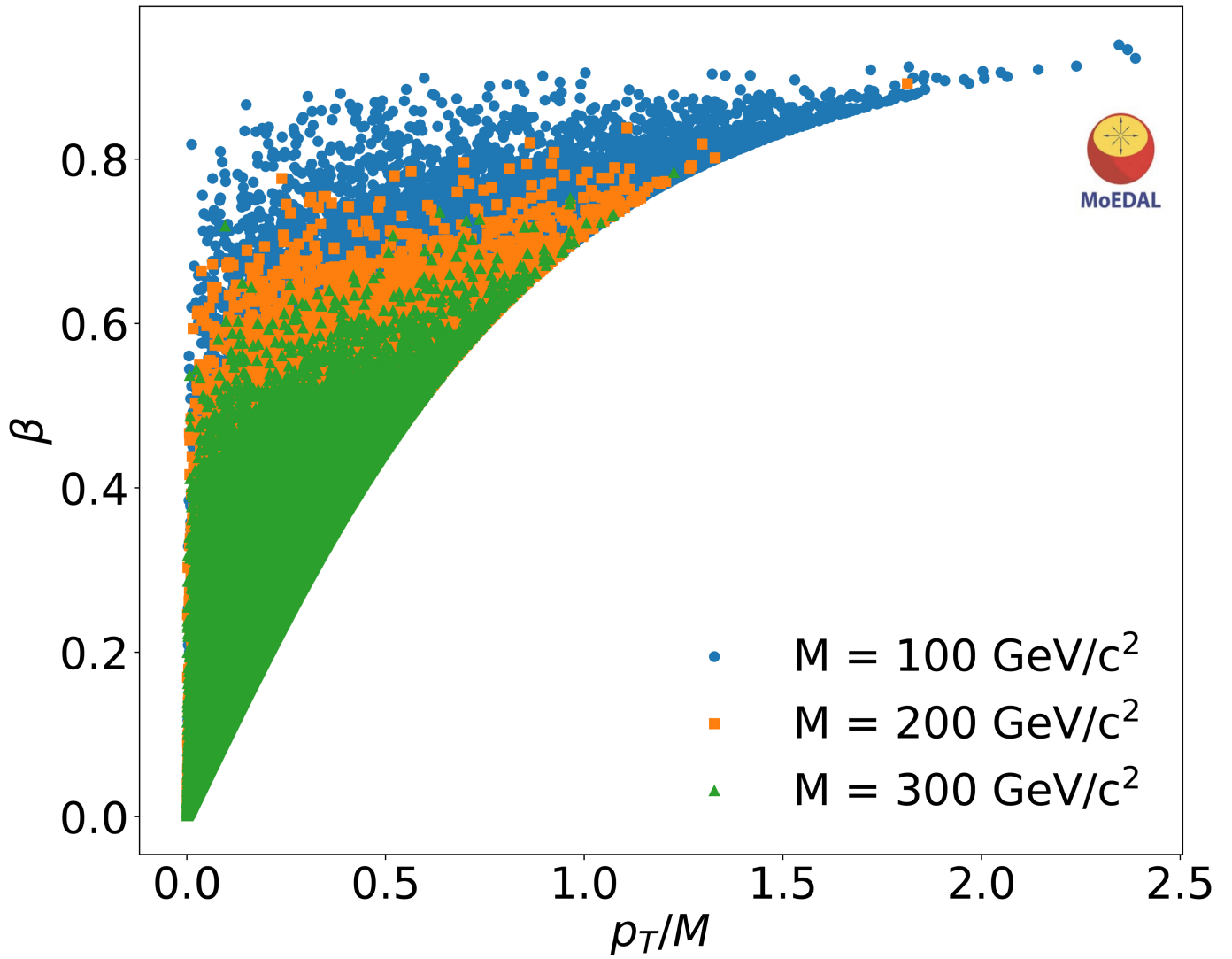
Peer review information *Nature* thanks Muneto Nitta, Steve Ahlen and the other, anonymous, reviewer(s) for their contribution to the peer review of this work.

Reprints and permissions information is available at <http://www.nature.com/reprints>.



Extended Data Fig. 1 | Mean expected rate of Schwinger MMs (R_{exp}). The mean expected rate of MMs with $1g_D$ (left) and $2g_D$ (right) magnetic charge in the MMT as a function of the MM mass in the FPA model. The black line

corresponds to the default geometry. The grey region corresponds to the systematic error, which is dominated by the material budget. The 95% confidence level mass exclusion region is shown in blue.



Extended Data Fig. 2 | Transverse momentum distribution of Schwinger MMs. The transverse momentum distribution for Schwinger MMs derived from the FPA, as a function of MM mass (M) plotted versus MM β .

Article

Extended Data Table 1 | Expected rate of MM trapping in the MoEDAL MMTs for the $1g_D$ FPA model, where ϵ is MMT trapping efficiency and R_{exp} is the mean expected rate of trapped MMs

M (GeV/c ²)	$ g $ (g_D)	σ (μb)	$\epsilon \cdot 10^{-4}$	R_{exp} (min-max)
50	1	$(2.0^{+0.5}_{-0.4}) \cdot 10^4$	$1.19^{+1.46}_{-0.64}$	$1.97 \cdot 10^2 - 1.50 \cdot 10^3$
75		$(6.6^{+2.0}_{-1.7}) \cdot 10^2$	$1.34^{+1.61}_{-0.72}$	7.13–59.5
80		$(2.0^{+0.7}_{-0.6}) \cdot 10^2$	$1.41^{+1.66}_{-0.76}$	2.23–19.5
85		$(1.2^{+0.3}_{-0.3}) \cdot 10^2$	$1.45^{+1.68}_{-0.78}$	1.30–11.5
100		$(4.0^{+1.5}_{-1.2}) \cdot 10^1$	$1.52^{+1.57}_{-0.83}$	0.45–4.16
105		$(2.4^{+0.9}_{-0.8}) \cdot 10^1$	$1.57^{+1.68}_{-0.82}$	0.29–2.51

Extended Data Table 2 | Expected rate of MM trapping in the MoEDAL MMTs for the $2g_D$ FPA model

M (GeV/c ²)	$ g $ (g_D)	σ (μb)	$\epsilon \cdot 10^{-7}$	R_{exp} (min-max)
50	2	$(3.1^{+0.8}_{-0.7}) \cdot 10^5$	$3.3^{+43}_{-3.0}$	$1.9\text{--}4.1 \cdot 10^2$
65		$(3.7^{+1.0}_{-0.9}) \cdot 10^4$	$3.8^{+48}_{-3.5}$	0.2–57
70		$(2.0^{+0.6}_{-0.5}) \cdot 10^4$	$3.8^{+50}_{-3.5}$	0.1–32
75		$(1.1^{+0.3}_{-0.3}) \cdot 10^4$	$4.5^{+51}_{-4.2}$	0.1–18
80		$(5.8^{+1.8}_{-1.6}) \cdot 10^3$	$4.3^{+49}_{-4.0}$	0.0–9.5
85		$(3.3^{+1.1}_{-0.9}) \cdot 10^3$	$4.4^{+50}_{-4.1}$	0.0–5.6

Extended Data Table 3 | Expected rate of MM trapping in the MoEDAL MMTs for the 3g₀ FPA model

M (GeV/c ²)	$ g $ (g_D)	σ (μb)	$\epsilon_{min-max}$	R_{exp} (min-max)
50	3	$(1.6_{-0.4}^{+0.4}) \cdot 10^6$	$< 1 \cdot 10^{-10} - 1.2 \cdot 10^{-6}$	0.0–5.3·10 ²
65		$(1.9_{-0.5}^{+0.6}) \cdot 10^5$	$< 1 \cdot 10^{-10} - 1.3 \cdot 10^{-6}$	0.0–75
70		$(9.9_{-2.5}^{+2.9}) \cdot 10^4$	$< 1 \cdot 10^{-10} - 1.2 \cdot 10^{-6}$	0.0–35
75		$(5.3_{-1.4}^{+1.6}) \cdot 10^4$	$< 1 \cdot 10^{-10} - 1.2 \cdot 10^{-6}$	0.0–19
80		$(2.9_{-0.8}^{+0.9}) \cdot 10^4$	$< 1 \cdot 10^{-10} - 1.3 \cdot 10^{-6}$	0.0–11
85		$(1.7_{-0.5}^{+0.6}) \cdot 10^4$	$< 1 \cdot 10^{-10} - 1.3 \cdot 10^{-6}$	0.0–6.6

Extended Data Table 4 | Expected rate of MM trapping in the MoEDAL MMTs for the $4g_b$ FPA model

M (GeV/ c^2)	$ g $ (g_D)	σ (μb)	$\epsilon_{min-max}$	R_{exp} (max-min)
50	4	$(5.0^{+1.2}_{-1.1}) \cdot 10^6$	$< 2 \cdot 10^{-9} - 3.5 \cdot 10^{-7}$	$0.0 - 5.1 \cdot 10^2$
65		$(6.0^{+1.7}_{-1.5}) \cdot 10^5$	$< 2 \cdot 10^{-9} - 3.9 \cdot 10^{-7}$	0.0–69
70		$(3.1^{+0.9}_{-0.8}) \cdot 10^5$	$< 2 \cdot 10^{-9} - 3.4 \cdot 10^{-7}$	0.0–32
85		$(1.7^{+0.5}_{-0.4}) \cdot 10^5$	$< 2 \cdot 10^{-9} - 2.8 \cdot 10^{-7}$	0.0–14
80		$(9.3^{+2.9}_{-2.5}) \cdot 10^4$	$< 2 \cdot 10^{-9} - 3.6 \cdot 10^{-7}$	0.0–10
85		$(5.2^{+1.7}_{-1.5}) \cdot 10^4$	$< 2 \cdot 10^{-9} - 3.6 \cdot 10^{-7}$	0.0–5.8

Extended Data Table 5 | Expected rate of MM trapping in the MoEDAL MMTs for the 5g₀ FPA model

M (GeV/c ²)	$ g $ (g_D)	σ (μb)	$\epsilon_{min-max}$	R_{exp} (max-min)
50	5	$(1.2^{+0.3}_{-0.3}) \cdot 10^7$	$< 2 \cdot 10^{-9} - 1.0 \cdot 10^{-7}$	$0.0 - 3.7 \cdot 10^2$
60		$(2.9^{+0.8}_{-0.7}) \cdot 10^6$	$< 2 \cdot 10^{-9} - 1.1 \cdot 10^{-7}$	0.0–93
65		$(1.5^{+0.4}_{-0.4}) \cdot 10^6$	$< 2 \cdot 10^{-9} - 1.4 \cdot 10^{-7}$	0.0–60
70		$(7.6^{+2.2}_{-1.9}) \cdot 10^5$	$< 2 \cdot 10^{-9} - 1.1 \cdot 10^{-7}$	0.0–25
75		$(4.1^{+1.3}_{-1.1}) \cdot 10^5$	$< 2 \cdot 10^{-9} - 1.0 \cdot 10^{-7}$	0.0–12
80		$(2.3^{+0.7}_{-0.6}) \cdot 10^5$	$< 2 \cdot 10^{-9} - 0.9 \cdot 10^{-7}$	0.0–6.4